# An actomyosin-polarized membrane reservoir mediates the unequal divisions of *Drosophila* neural stem cells

Bryce LaFoya and Kenneth E. Prehoda

Institute of Molecular Biology
Department of Chemistry and Biochemistry
1229 University of Oregon
Eugene, OR 97403

Corresponding author: prehoda@uoregon.edu

## Summary

The asymmetric divisions of *Drosophila* neural stem cells (NSCs) produce unequally sized siblings, with most volume directed into the sibling that retains the NSC fate. Sibling size asymmetry results from preferential expansion of the NSC sibling surface during division. Here we show that a polarized membrane reservoir constructed by the NSC in early mitosis provides the source for expansion. The reservoir is formed from membrane domains that contain folds and microvilli that become polarized by apically-directed cortical flows of actomyosin early in mitosis. When furrow ingression begins and internal pressure increases, the stores of membrane within the apical reservoir are rapidly consumed. Expansion is significantly diminished in NSCs that lack a reservoir, and membrane expansion equalizes when the reservoir is not polarized. Our results suggest that the cortical flows that remodel the plasma membrane during asymmetric cell division function to satisfy the dynamic surface area requirements of unequally dividing cells.

## Introduction

Cellular resources can be partitioned unequally during division to facilitate differences in sibling cell fate and proliferation potential. For example, dividing *Drosophila* neural stem cells (NSCs) direct most cell volume into the sibling that retains the NSC fate and remains highly proliferative. In contrast, the neural precursor (NP) sibling that is destined towards differentiation and a postmitotic state receives a small fraction of the total volume (Gallaud et al., 2017; Homem and Knoblich, 2012). While asymmetric spindle positioning can contribute to unequal cell division, the size asymmetry of the NSC and NP cells results from preferential expansion of the nascent NSC surface during anaphase (Cabernard et al., 2010; Connell et al., 2011; Pham et al., 2019; Roubinet et al., 2017). Biased expansion is characterized by a rapid increase in surface area near the NSC pole while the area near the other pole remains relatively constant (Connell et al., 2011). Expansion occurs when intracellular hydrostatic pressure increases following the initiation of furrow ingression (Pham et al., 2019). While a biased increase in surface area is a key aspect of the unequal NSC division, little is known about how the plasma membrane accommodates asymmetric polar expansion. Here we examine the plasma membrane dynamics that support the geometric changes that accompany the unequal NSC division.

Morphological changes can significantly alter cell surface area, placing significant demands on the plasma membrane. Many animal cells, including the NSC, become spherical before

dividing, a geometry that uses surface area most efficiently for a given volume. Division can lead to rapid morphology changes, including elongation and furrow ingression, that can quickly increase surface area as the cell assumes a non-spherical shape. However, the plasma membrane is relatively inelastic and can only undergo limited stretching to accommodate increases in surface area. One mechanism that cells use to buffer changes in surface area is to store membrane in cell surface reservoirs (Figard et al., 2013; Figard and Sokac, 2014; Kabeche et al., 2015). Membrane reservoirs use folds and microvilli to store membrane that is unnecessary for encapsulating the cell (i.e. excess membrane). Changes in cell shape that increase surface area, like those that accompany division, can be accommodated by tapping into the reservoir, in turn reducing the amount of excess membrane.

The NSC undergoes large, highly asymmetric morphological changes during division. Although it is not known to contain a reservoir, the NSC membrane is very dynamic, undergoing a polarity cycle that resembles its well-characterized protein polarity cycle (LaFoya and Prehoda, 2021). During the protein cycle, polarity proteins and fate determinants become polarized to the NSC's apical and basal hemispheres during early mitosis (Gallaud et al., 2017; Homem and Knoblich, 2012; Knoblich, 2010, 2008). The apical proteins are polarized in part by apically-directed cortical flows of actomyosin. These cortical movements lead to the formation of an organized cap near the apical pole that remains until it depolarizes shortly before division (Oon and Prehoda, 2021, 2019). The plasma membrane undergoes a similar cycle in which membrane features that are initially dispersed over the surface of the cell move apically, in synchrony with polarity proteins, before appearing to spread over the surface by moving basally during anaphase (LaFoya and Prehoda, 2021). The dynamic NSC membrane features can be detected with diverse membrane markers and some are clearly microvilli suggesting that they could store excess membrane. Here we examine whether the NSC membrane contains a reservoir and if so, how membrane dynamics might contribute to the biased expansion that mediates unequal NSC division.

## Results

### The apparent surface area of the apical NSC sibling increases during division

We first estimated the demand on the plasma membrane during the divisions of *Drosophila* larval brain NSCs (Figure 1A). Like many animal cells, NSCs become spherical in early mitosis and the sibling cells remain spherical following the completion of furrowing (Figure 1B). The difference between the surface area required to encapsulate the NSC before division (e.g. at

65 metaphase) and that for both siblings represents the amount of additional plasma membrane
66 surface area required for the division. We term the surface area required to encapsulate the cell
67 the *apparent surface area,* as the plasma membrane can store a reservoir of additional surface
68 area in membrane fine structure such as folds and microvilli, which we term *excess membrane*
69 (Figure 1C). We measured the overall increase in apparent surface area using Miranda-GFP,
70 which marks the surface area of the nascent NP and NP siblings directly (with membrane-
71 bound signal), and the nascent NSC and NSC sibling indirectly (with cytoplasmic signal; Figure
72 1D) (Ramat et al., 2017). We found that the apparent surface area increased by an average of
73 74 ± 19 $\mu m^2$ (n = 10; mean ± SD) from metaphase to the completion of furrowing. We also used
74 this method to estimate the bias in apparent surface area change between NSC and NP
75 siblings, with the caveat that Miranda-GFP's demarcation between NSC and NP may change
76 slightly over this time frame. Consistent with previous measurements using the change in cell
77 length along the division axis (Connell et al., 2011; Pham et al., 2019; Roubinet et al., 2017), we
78 found that expansion is highly asymmetric, with an average increase of 94 ± 17 $\mu m^2$ for the
79 NSC apparent surface area and a relatively small but significant decrease of -20 ± 10 $\mu m^2$ for
80 the NP cell (n = 10; Figure 1E). The decrease may arise from shrinking of the Miranda-GFP
81 domain but nevertheless indicates that the overall increase in surface area is mediated
82 primarily by expansion of the nascent NSC surface. We conclude that the NSC division creates
83 a significant demand for new surface area that is satisfied by a biased expansion process that
84 directs the increase in surface area primarily towards the future NSC sibling.

85 **Neural stem cell membrane domains are a reservoir of excess membrane**

86 We sought to understand how the NSC satisfies the requirement for additional surface area
87 during division and the mechanism by which it is biased towards the NSC rather than the NP
88 sibling. The NSC membrane is heterogeneous, with distinct domains characterized by localized
89 areas of relatively high membrane marker intensity (Figure 1F) (LaFoya and Prehoda, 2021).
90 NSC membrane domains are distributed across the cell surface in interphase and early mitosis
91 and can be detected with diverse membrane markers. The higher marker intensity within NSC
92 membrane domains could arise from an increased density of specific membrane components
93 in a single bilayer (Figure 1G-scheme 1). Alternately, increased amounts of plasma membrane
94 in the form of folds or microvilli could also lead to higher marker intensity (Figure 1G-scheme
95 2), and some microvilli are known to be present (LaFoya and Prehoda, 2021). We examined the
96 prevalence of excess membrane in membrane domains by measuring their thickness using

97 super resolution imaging (Azuma and Kei, 2015). NSC membrane domains in regions without
98 signal from surrounding cells were nearly exclusively associated with increased thickness
99 relative to adjacent membrane, which had a relatively uniform thickness approximately equal to
100 the diffraction limited width (Figure 1H). Furthermore, many membrane domains colocalized
101 with activated Moesin, a marker for microvilli (Fehon et al., 2010) (Figure 1I). We conclude that
102 excess membrane is stored on the NSC surface in discrete regions that are thicker than
103 surrounding regions and often contain microvilli. The presence of excess membrane makes the
104 total NSC membrane surface area greater than the apparent surface area of the cell body, a
105 phenomenon that has been compared to the "coastline paradox" in which the size of an
106 interface is influenced by the presence of structure at different length scales (Sokac, 2017).

107 **Excess plasma membrane moves apically to form a polarized membrane reservoir**

108 NSC membrane domains that are dispersed over the cell surface in early mitosis become
109 concentrated around the apical pole by metaphase (Figure 2A and Video S1) (LaFoya and
110 Prehoda, 2021). Given our finding that membrane domains store excess membrane, we
111 hypothesized that the polarization process causes excess membrane to accumulate
112 specifically to the apical pole. Consistent with this hypothesis, we measured a significant
113 increase in apical membrane structure thickness at metaphase compared to prophase (Figure
114 2B). We did not detect any basally-directed movement of excess membrane during this time
115 period, nor did we detect an increase in the membrane structure's thickness at the basal pole
116 (Figure 2B, Video S1). We also observed deformation of domains along the apical-basal axis as
117 they moved towards the apical pole (c.f. Figure 2A inset, Video S1), suggesting the presence of
118 tension-induced deformation of the membrane structures. Cell contacts between the NSC and
119 adjacent progeny cells also undergo a similar pattern of deformation along the apical-basal
120 axis indicating the presence of extensive mechanical forces which polarize the NSC surface in
121 early mitosis (Figure 2A and Video S1) (LaFoya and Prehoda, 2021). We conclude that the
122 polarization of the NSC membrane occurs at least in part from accumulation of excess
123 membrane near the apical pole due to directional transport from around the cell surface.

124 **Cortical actomyosin flows drive apical plasma membrane accumulation**

125 The apically-directed membrane domain movements that construct the polarized membrane
126 reservoir do not occur in Latrunculin A-treated NSCs (LaFoya and Prehoda, 2021), indicating
127 that they require F-Actin. Furthermore, apically-directed cortical flows of actomyosin in
128 prophase NSCs have recently been reported (Oon and Prehoda, 2021), suggesting that cortical

129 flows could drive the formation of the apical membrane reservoir. We examined whether
130 cortical cytoskeletal flows are correlated with membrane polarization dynamics using super
131 resolution, simultaneous imaging of the membrane and F-Actin, and separately membrane and
132 Myosin II (Figure 3). As previously reported (LaFoya and Prehoda, 2021), we observed
133 enrichment of F-Actin at sites of excess membrane (Figure 3 and Video S2). Here we find that
134 the movements that polarize membrane domains are highly correlated with those of the cortical
135 F-Actin meshwork that lies outside of the domains (Figure 3A,B and Video S2). We also
136 examined the dynamics of Myosin II and did not observe its colocalization with membrane
137 domains (Figure 3C and Video S3). However, the apically-directed movements of cortical
138 Myosin II during prophase were strongly correlated with membrane domain movements that
139 form the apical reservoir (Figure 3C,D and Video S3).

140 The correlated motions of actomyosin and membrane suggest that actomyosin cortical flows
141 are responsible for constructing the apical membrane reservoir. We tested this model by
142 inhibiting Myosin II with the Rho Kinase inhibitor Y27632. While Y27632 can also inhibit the
143 polarity kinase aPKC (Atwood and Prehoda, 2009), aPKC activity is not required for apical
144 movements of membrane domains (LaFoya and Prehoda, 2021). We found that addition of
145 Y27632 inhibited domain movement leading to failure to establish the apical membrane
146 reservoir (Figure 4A-C and Video S4). Our results indicate that NSC membrane domains
147 contain Actin and activated Moesin (Figure 1I), but not Myosin II (Figure 3C), and that the
148 domains move apically during prophase with dynamics that are highly correlated with
149 actomyosin cortical flows and that require Myosin II activity (Figure 4D).

150 **Consumption of apical membrane reservoir during NSC division**

151 The NSC constructs a polarized membrane reservoir in early mitosis by moving excess
152 membrane to the apical pole using actomyosin driven cortical flows. How might the NSC use
153 this structure to accommodate the rapid morphological changes that occur in late mitosis? We
154 examined the dynamics of the apical membrane reservoir during anaphase, when the apical
155 region's apparent surface area increases (Figure 1E) (Connell et al., 2011; Pham et al., 2019).
156 The internal pressure of the NSC changes dramatically during this phase of the cell cycle,
157 peaking shortly after furrow ingression followed by a rapid decrease that coincides with
158 membrane expansion (Pham et al., 2019). We followed the dynamics of the apical membrane
159 reservoir during anaphase using super resolution imaging with high temporal resolution. We
160 observed thinning of the apical membrane structure that coincided with the morphological

161 changes associated with late mitosis (cell elongation and furrow ingression), and the increase
162 in apical surface area (Figure 5 and Video S5; the full formation and consumption process is
163 shown in Video S6). Microvilli that extended over a micron from the cell surface were
164 reabsorbed into the cell as furrowing continued (Figure 5A and Video S5). As membrane
165 reservoir consumption occurred, the apical surface expanded and the remaining domains of
166 excess membrane appeared to move basally (Figure 5B), leading to a decrease in membrane
167 structure thickness at the apical pole but no detectable change at the basal pole (Figure 5C).
168 To ensure that the apical membrane structure thickness decrease was not simply a
169 consequence of domains moving out of the focal plane, we monitored the maximum thickness
170 of individual domains over time across optical sections and observed a significant decrease
171 beginning at anaphase onset (Figure 5D). Both F-Actin (Figure 5E and Video S7) and Myosin II
172 (Figure 5F and Video S8) migrated towards the cleavage furrow during this time period, as
173 previously described (Roth et al., 2015; Roubinet et al., 2017). Thus, NSCs construct a
174 polarized membrane reservoir in early metaphase that is consumed late in mitosis as the apical
175 membrane expands.

176 **The membrane reservoir is required for expansion and completion of cytokinesis**

177 Our data indicate that the apical membrane reservoir is consumed during anaphase,
178 suggesting that the reservoir mediates preferential expansion at the apical pole. To investigate
179 how the NSC division process proceeds without a reservoir, we examined the divisions of
180 cyclodextrin-treated NSCs. Cyclodextrin treatment can ablate membrane domains in diverse
181 cell types (Barman and Nayak, 2007; Pang et al., 2007), perhaps because it extracts
182 cholesterol, significantly decreasing membrane rigidity (Chakraborty et al., 2020). In previous
183 work, we found that cyclodextrin treatment inhibits formation of NSC membrane features
184 (LaFoya and Prehoda, 2021). Consistent with previous observations, we found that the
185 membranes of cyclodextrin-treated NSCs were relatively featureless such that the plasma
186 membrane smoothly followed the contours of the cell (Figure 6A), apparently lacking any
187 excess membrane. In the absence of a membrane reservoir, very little polar expansion
188 occurred, and furrowing was incomplete and unstable (Figure 6B,C and Video S9). The failure
189 to robustly furrow is consistent with a model in which the NSC reservoir provides the
190 membrane necessary for the apparent surface area increase during division (Figard et al., 2016;
191 Figard and Sokac, 2014). However, it is also possible that the cytokinesis defect arises at least

192 in part from another effect of the cyclodextrin treatment, such as its effect on membrane
193 rigidity.

194 **Membrane reservoir polarization is required for biased expansion**

195 Our data suggest that membrane reservoir polarization mediates biased expansion during NSC
196 division. We examined how failure to polarize the membrane reservoir influences expansion
197 using NSCs expressing RNAi directed against the heterotrimeric G-protein Gγ1 (hereafter Gγ).
198 Gγ is known to be required for asymmetric NSC division (Izumi et al., 2004), and we found that,
199 unlike wild-type NSCs, NSCs expressing Gγ RNAi do not polarize their membranes in early
200 mitosis (Figure 7 and Video S10). In early mitosis, cells expressing Gγ RNAi had excess
201 membrane distributed over their surface, like their wild-type counterparts. However, the
202 apically-directed movements that polarize the membrane reservoir of wild-type NSCs failed to
203 occur in Gγ RNAi-expressing cells. Without these polarizing movements, these cells failed to
204 form a membrane reservoir at the apical pole as excess membrane remained distributed
205 across the cell surface as furrow ingression commenced (Figure 7C). In the absence of a
206 polarized membrane reservoir, the expansion that occurred following ingression was equally
207 distributed to both poles and daughter cell size was approximately symmetric. We conclude
208 that the biased expansion of the NSC membrane is mediated by polarization of the membrane
209 reservoir before division.

210 **Discussion**

211 The morphological changes that accompany cell division can place significant demands on the
212 plasma membrane by rapidly increasing total surface area. During the unequal divisions of
213 *Drosophila* NSCs, the surface area increase is biased, with the nascent NSC surface expanding
214 as the furrow ingresses while the NP surface remains relatively constant (Figure 1E) (Connell et
215 al., 2011; Pham et al., 2019). In general, the demand for membrane can be buffered by
216 reservoirs of excess membrane stored in folds and microvilli, or eisosomes in yeast (Figard et
217 al., 2016; Figard and Sokac, 2014; Goudarzi et al., 2017; Kabeche et al., 2015). We discovered
218 a membrane reservoir that mediates the biased expansion that occurs during NSC asymmetric
219 division (Figure 8). The reservoir is constructed from localized regions of excess membrane
220 that are dynamically collected at the apical pole by apically-directed cortical flows of
221 actomyosin that begin and end in early mitosis (Figure 3) (Oon and Prehoda, 2021). When the
222 apical membrane starts expanding as cell elongation and cleavage furrow ingression
223 commence, the excess membrane in the reservoir begins incorporating into the membrane that

224 encapsulates the cell body. Expansion and reservoir consumption coincide with the drop in
225 internal hydrostatic pressure that occurs during anaphase (Pham et al., 2019). Our results
226 indicate that NSC membrane structures play a specific role in accommodating the rapid
227 surface area changes that occur in the late phases of mitosis, but it is important to note that
228 they do not exclude a role for these structures in other processes, such as in mediating
229 intercellular signaling like cytonemes (Kornberg, 2014).

230 Examination of NSC membrane dynamics revealed that the cell goes to great lengths to
231 prepare for biased expansion, generating directional cortical flows to collect excess membrane
232 at the apical pole (Figure 2). Directional cortical flows of actomyosin play a role in the
233 polarization of both the plasma membrane and proteins during the NSC division (LaFoya and
234 Prehoda, 2021; Oon and Prehoda, 2021, 2019), and their role in cortical protein polarity of the
235 asymmetrically-dividing *C. elegans* zygote has been extensively studied (Illukkumbura et al.,
236 2019; Lang and Munro, 2017; Munro et al., 2004). Furthermore, polarized membrane structures
237 have also been reported in the zygote (Hirani et al., 2019; Scholze et al., 2018), suggesting that
238 they may play a more general role in asymmetric division. While cortical movements of polarity
239 proteins such as aPKC are driven by actomyosin cortical flows in the NSC, F-Actin is not
240 strictly required for its polarity. For example, in Latrunculin A treated NSCs that lack an Actin
241 cytoskeleton, aPKC polarizes but ultimately diffuses into the basal hemisphere (Oon and
242 Prehoda, 2019). Thus, currently available data suggest that actomyosin cortical flows in the
243 NSC function primarily to organize the membrane and are not essential for establishing protein
244 polarity, even while the cortical cytoskeleton maintains protein polarity by preventing spreading
245 into the basal hemisphere (LaFoya and Prehoda, 2021; Oon and Prehoda, 2019).

246 How might actomyosin-generated cortical flows be coupled to the directional movement of
247 excess membrane domains? Our results suggest a specific mechanism (Figure 4D). Membrane
248 domains contain F-Actin that is coupled to the membrane via activated Moesin. This allows for
249 direct coupling to the cortical cytoskeleton which undergoes apically-directed movements in
250 early prophase (Figure 3) (Oon and Prehoda, 2021). This mechanism is similar to one described
251 for cultured mammalian epithelial cells, in which microvilli move rapidly across the cell surface
252 to form the brush border (Meenderink et al., 2019). Microvillar movement in both systems is
253 based on coupling between F-Actin in microvilli and the cortical actomyosin cytoskeleton. In
254 the developing brush border, however, microvillar motion is driven primarily by treadmilling of
255 an interior Actin bundle. In contrast, movement of microvilli on the NSC surface is coupled to

256 apically directed cortical flows of actomyosin (Figures 3,4). The NSC cortical flows are coupled
257 not only to the movements of excess membrane, but also to the surrounding tissue (LaFoya
258 and Prehoda, 2021; Oon and Prehoda, 2021), suggesting connections to a broad range of
259 membrane-associated structures, including adhesions.

260 Shortly after its formation, the apical reservoir is tapped during anaphase (Figure 5), coinciding
261 with the onset of furrow ingression and the peak of internal hydrostatic pressure (Pham et al.,
262 2019). Simultaneously with these processes, Myosin II redistributes from the apical pole
263 towards the cleavage furrow (Oon and Prehoda, 2021; Pham et al., 2019; Roubinet et al.,
264 2017). Reservoir consumption could be caused by Myosin II relocalization or the initiation of
265 furrow ingression, or a combination of both processes. Alternately redistribution of Myosin II
266 could be a mechanical consequence of reservoir tapping.

267 **Acknowledgments**
268 This work was supported by NIH grants GM127092 and F32GM134705.

269 **Figure Legends**
270 Figure 1 Neural stem cell membrane domains store excess membrane

271 (A) *Drosophila* larval central nervous system explants used in this study. Larval brain lobe
272 neural stem cells were imaged from explants dissected from third instar larvae (vnc: ventral
273 nerve cord).

274 (B) Model for the unequal division of neural stem cells. Preferential expansion of the apical
275 hemisphere during anaphase contributes to size asymmetry. The goal of this study was to
276 identify the membrane source for biased expansion. NSC = neural stem cell. NP = neural
277 progenitor.

278 (C) Apparent surface area and excess membrane. The total plasma membrane surface area is
279 the sum of the surface area required to encapsulate the cell body ("apparent surface area") and
280 the surface area of membrane structures such as folds and microvilli ("excess membrane").

281 (D) Use of the NP marker Miranda (Miranda-GFP expressed from its endogenous locus) to
282 measure NSC and NP apparent surface areas from metaphase ("meta"; immediately prior to
283 cell elongation) and the completion of observable furrowing ("cyto"; cytokinesis). Dashed red

284 lines show the demarcation of NSC and NP and “a-b” denotes apical-basal axis. A medial
285 section of the NSC along the apical-basal axis is shown for each time point.

286 (E) Change in apparent surface area that accompanies NSC division. The difference in
287 apparent surface area from metaphase (“meta”) to the completion of observable furrowing
288 (“cyto”; cytokinesis) is shown for divisions of 10 different NSCs using Miranda-GFP to mark the
289 NSC and NP sibling surfaces.

290 (F) Examples of NSC membrane structure associated with localized regions of increased
291 membrane marker intensity (”a-b” denotes apical-basal axis). The membrane marker is
292 expressed in neural stem cells and their progeny (worniu-GAL4>UAS-farnesyl-GFP). A three-
293 dimensional projection of the front hemisphere of the NISC and adjacent progeny cells is
294 shown (top-left panel) adjacent to a close up of the NSC surface (top-right panel). A medial
295 section along the apical-basal axis is shown in the bottom-left adjacent to a close up of the
296 NSC surface (bottom-right).

297 (G) Schemes for localized enrichment of membrane marker: 1) a configuration that yields a
298 localized increase in membrane marker concentration by increased density on a single plasma
299 membrane. 2) a configuration that yields a localized increase in intensity with uniform
300 membrane marker concentration but increased membrane density.

301 (H) Variation of NSC membrane thickness associated with localized regions of increased
302 membrane marker intensity (worniu-GAL4>UAS-farnesyl-GFP; “membrane”). The structural
303 thickness of the membrane at regions inside and outside of membrane domains (n = 28) is
304 plotted in a Gardner-Altman estimation plot. The 95% confidence interval is shown along with
305 the bootstrap estimation distribution. The inset depicts an example structural thickness
306 measurement.

307 (I) Colocalization of activated Moesin with membrane structures. A neural stem cell expressing
308 the membrane marker worniu-GAL4>UAS-PLCδ-PH-GFP fixed and stained with anti-GFP
309 (“membrane”) and anti-activated Moesin (“p-Moesin”; phosphorylated Moesin). A three-
310 dimensional projection of the front hemisphere of the NSC is shown.

311 Figure 2 Apically directed membrane domain movements during prophase form an apical
312 membrane reservoir

313 (A) Frames from Video S1 showing the apically directed movement of excess membrane during
314 prophase that leads to the accumulation of excess membrane near the apical pole at
315 metaphase. Membrane is marked by worniu-GAL4>UAS-PLCδ-PH-GFP. The first row shows a
316 three-dimensional projection for each time point, with arrow heads tracking one membrane
317 domain as it moves apically. The second row shows an inset (box in first row) highlighting the
318 membrane domain tracked in the first row. The third row shows a medial section for each time
319 point. Time is shown relative to anaphase onset (m:ss) and "a-b" denotes the apical-basal axis.

320 (B) Change in membrane structure thickness increases at the apical and basal poles between
321 ten minutes and one minute prior to anaphase onset. A Gardner-Altman estimation plot is
322 shown for the change in membrane thickness structure for apical and basal poles (n = 5
323 NSCs). The 95% confidence interval is shown along with the bootstrap estimation distribution.
324 Insets show example measurements of membrane thickness at each pole.

325 Figure 3 Apically directed flows of cortical actomyosin are correlated with the movement of
326 excess membrane towards the apical pole

327 (A) Selected frames from Video S2 showing coordinated movement of cortical F-Actin (worniu-
328 GAL4>UAS-GMA [GFP-Moesin Actin binding domain]; "F-Actin") and excess membrane
329 domains (worniu-GAL4>UAS-PLCδ-PH-mCherry; "membrane"). A three-dimensional projection
330 is shown for each time point. Time is shown relative to anaphase onset (m:ss) and "a-b"
331 denotes apical-basal axis.

332 (B) Coordinated movements of cortical Actin and membrane domains. Inset as shown from
333 panel A with arrows highlighting moving membrane domain and cortical Actin mesh.

334 (C) Selected frames from Video S3 showing coordinated movement of Myosin II (Sqh-GFP
335 [Spaghetti Squash; *Drosophila* Myosin II regulatory light chain]; "Myosin II") and excess
336 membrane domains (worniu-GAL4>UAS-PLCδ-PH-mCherry; "membrane"). A three-
337 dimensional projection is shown for each time point. Time is shown relative to anaphase onset
338 (m:ss) and "a-b" denotes apical-basal axis.

339 (D) Coordinated movements of cortical Myosin II and membrane domains. Inset as shown from
340 panel C with arrows highlighting moving membrane domain and cortical Myosin II puncta.

341 Figure 4 Activity of the Myosin II regulator Rho Kinase is required for NSC membrane
342 polarization

343 (A) Frames from Video S4 showing the effect of the Rho Kinase inhibitor (Y27632) on
344 membrane reservoir formation. Membrane is marked by worniu-GAL4>UAS-PLCδ-PH-GFP
345 and microtubules are marked by worniu-GAL4>UAS-Zeus-mCherry. A three-dimensional
346 projection is shown for each time point. Time is shown relative to anaphase onset (mm:ss) and
347 "a-b" denotes apical-basal axis.

348 (B) Frames from Video S4 showing the effect of the vehicle DMSO on membrane reservoir
349 formation. Membrane is marked by worniu-GAL4>UAS-PLCδ-PH-GFP and microtubules are
350 marked by worniu-GAL4>UAS-Zeus-mCherry. Time is shown relative to anaphase onset (m:ss)
351 and "a-b" denotes apical-basal axis.

352 (C) Rho kinase activity is required for the increase in apical membrane thickness. A Gardner-
353 Altman estimation plot is shown for the change in apical membrane thickness in treated
354 (vehicle + Y27632) and untreated (vehicle only) cells. The 95% confidence interval is shown
355 along with the bootstrap estimation distribution.

356 (D) Model for membrane reservoir polarization. Excess membrane is contained in membrane
357 fine structure such as microvilli that contain F-Actin and activated Moesin. Apically-directed
358 flows of the cortical actomyosin cytoskeleton lead to coordinated movement of excess
359 membrane domains towards the apical pole.

360 Figure 5 Consumption of the apical membrane reservoir during anaphase expansion

361 (A) Frames from Video S5 showing the consumption of the apical membrane reservoir through
362 anaphase and furrow ingression. Membrane is marked by worniu-GAL4>UAS-PLCδ-PH-GFP.
363 The first row shows a three-dimensional projection, the second row shows a medial section for
364 each time point, and the third row shows the inset specified by the box in the second row.
365 Arrows show microvilli as it is absorbed into the cell body. Time is shown relative to anaphase
366 onset (m:ss) and "a-b" denotes apical-basal axis.

367 (B) Straightened membrane sections from Video S5 showing the apical pole to the furrow at
368 times relative to anaphase onset.

369 (C) Change in membrane structure thickness at the apical and basal poles between metaphase
370 and the completion of furrowing. A Gardner-Altman estimation plot is shown for membrane
371 structure thickness change at both locations. The 95% confidence interval is shown along with
372 the bootstrap estimation distribution.

373 (D) Membrane domain consumption dynamics during anaphase. The maximum membrane
374 structure thickness (across x, y, and z) for individual domains (n = 15) is shown as a function of
375 time relative to anaphase onset. The thickness is normalized to the starting value. The line
376 represents the mean and the shaded region is one standard deviation.

377 (E) F-Actin dynamics during anaphase membrane reservoir consumption. Selected frames from
378 Video S7 showing coordinated movement of cortical F-Actin (worniu-GAL4>UAS-GMA; "F-
379 Actin") and excess membrane domains (worniu-GAL4>UAS-PLCδ-PH-GFP; "membrane").
380 Time is shown relative to anaphase onset (m:ss) and "a-b" denotes apical-basal axis.

381 (F) Myosin II dynamics during anaphase membrane reservoir consumption. Selected frames
382 from Video S8 showing coordinated movement of Myosin II (Sqh-GFP; "Myosin II") and excess
383 membrane domains (worniu-GAL4>UAS-PLCδ-PH-mCherry; "membrane"). Time is shown
384 relative to anaphase onset (m:ss) and "a-b" denotes apical-basal axis.

385 Figure 6 Cyclodextrin treatment removes excess membrane

386 (A) The effect of Methyl-β-cyclodextrin ("cyclodextrin") treatment on the NSC membrane
387 (marked by worniu-GAL4>UAS-PLCδ-PH-GFP). A three-dimensional projection and a medial
388 section is shown.

389 (B) Effect of cyclodextrin treatment on cytokinesis. "Completion" denotes cells that completed
390 furrowing whereas "failure" denotes cells whose furrow failed to completely ingress. Outcomes
391 of cytokinesis for untreated NSCs are compared to cyclodextrin treated NSCs.

392 (C) Selected frames from Video S9 showing the effect of cyclodextrin treatment on the NSC
393 membrane and cytokinesis. Membrane is marked by worniu-GAL4>UAS-PLCδ-PH-GFP and
394 microtubules are marked by worniu-GAL4>UAS-Zeus-mCherry. Arrows mark furrow that
395 initially ingresses and ultimately retracts. Time is shown relative to anaphase onset (mm:ss) and
396 "a-b" denotes apical-basal axis.

397 Figure 7 Membrane reservoir asymmetry is required for biased expansion

398 (A) Selected frames from Video S10 of an NSC expressing RNAi directed against Gγ1 and the
399 membrane marker UAS-PLCδ-PH-GFP (worniu-GAL4>UAS-PLCδ-PH-GFP; "membrane"). A
400 three-dimensional projection and a medial section is shown for each time point. Time is shown
401 relative to anaphase onset (m:ss) and "a-b" denotes apical-basal axis.

402 (B) Selected frames from Video S6 of a wild type NSC expressing the membrane marker
403 worniu-GAL4>UAS-PLCδ-PH-GFP for comparison. A three-dimensional projection and a
404 medial section is shown for each time point. Time is shown relative to anaphase onset (m:ss)
405 and "a-b" denotes apical-basal axis.

406 (C) Membrane structure thickness changes at the apical and basal poles 10 minutes and 1
407 minute prior to anaphase onset in NSCs expressing RNAi directed against Gγi. A Gardner-
408 Altman estimation plot is shown for the change in membrane structure thickness at the apical
409 and basal poles (n = 5 NSCs). The 95% confidence interval is shown along with the bootstrap
410 estimation distribution.

411 Figure 8 Model for reservoir-mediated asymmetric cell division

412 In early mitosis, excess membrane contained within folds and microvilli are distributed across
413 the cell surface. Apically-directed movements of membrane domains, mediated by directional
414 flows of cortical actomyosin, lead to accumulation of the domains at the apical pole and the
415 formation of an apical reservoir of excess membrane. The expansion that occurs at the apical
416 pole, and creates the larger NSC sibling, is accompanied by consumption of the reservoir.

## Star Methods

### Resource Availability

#### *Lead Contact*

Further information and requests for resources and reagents should be directed to the Lead Contact, Kenneth Prehoda (prehoda@uoregon.edu).

#### *Materials Availability*

This study did not generate new unique reagents.

#### *Data and Code Availability*

The raw data supporting the current study have not been deposited in a public repository because of their large file size, but are available from the corresponding author on request.

### Experimental Model and Subject Details

#### *Fly Strains*

For tissue specific expression of UAS controlled transgenes in NSCs, a Worniu-GAL4 driver line was used. For live imaging of membrane dynamics, two different classes of membrane-bound fusion proteins were used, both of which nearly exclusively label the plasma membrane and not internal membranes in NSCs. UAS-farnesyl-GFP expresses the C-terminal region of human K-Ras tagged with GFP which becomes farnesylated and plasma membrane-anchored in cells. UAS-PLCδ-PH-GFP and UAS-PLCδ-PH-mCherry express the pleckstrin homology domain of human PLCδ tagged with GFP or mCherry, and binds to the plasma membrane lipid phosphoinositide PI(4,5)$P_2$. F-Actin was imaged using UAS-GMA-GFP, which expresses the Actin binding domain of Moesin tagged with GFP. Progression through mitosis was tracked by expressing the microtubule marker UAS-Zeus-mCherry in NSCs, which labels microtubules allowing the visualization of the mitotic spindle. Symmetrical cell division in NSCs was induced through the expression of dsRNAi of G protein γ1 (Gγ1, FBgn0004921) under UAS control. Miranda-GFP expresses GFP tagged Miranda at the endogenous loci (Ramat et al., 2017).

446 Myosin II was imaged using GFP tagged Spaghetti squash (Sqh), the regulatory light chain of
447 Myosin II, expressed from the natural promoter (Royou et al., 2002).
448
449 **Method Details**
450 ***Live Imaging***
451 Intact *Drosophila* central nervous systems were dissected from third instar larvae in a bath of
452 Schneider's Insect Media (SIM). These larval brain explants were then mounted dorsal side
453 down on sterile poly-D-lysine coated 35mm glass bottom dishes (ibidi Cat#81156) containing
454 modified minimal hemolymph-like solution (HL3.1). Explants were imaged on a Nikon Eclipse
455 Ti-2 (60x $H_2O$ objective) equipped with a Yokogawa CSU-W1 SoRa spinning disk head and
456 dual Photometrics Prime BSI sCMOS cameras. GFP tagged proteins were illuminated with
457 488nm. Proteins tagged with mCherry were illuminated with 561nm laser light. For super
458 resolution imaging, individual NSCs were imaged using SoRa optics which achieve super
459 resolution through optical photon reassignment. For time lapse super resolution imaging,
460 images were acquired every 2-60 seconds. All figures and videos depict super resolution
461 images, except in Video S10 where NSC #2 and #3 were captured using standard resolution
462 imaging. For standard resolution time lapse imaging a z-stack of 41-61 optical sections with a
463 step size of 0.5 μm was acquired every 10-20 seconds. For z-stacks acquired during super
464 resolution imaging, a step size of 0.3 μm was used. Where time relative to anaphase onset is
465 noted, anaphase onset was identified as the frame in which the apical membrane begins its
466 expansion which coincides with the separation of the sister chromatids (LaFoya and Prehoda,
467 2021). To examine the effects of Rho Kinase inhibition on membrane dynamics, explants were
468 treated with 1 mM Y27632 (solubilized in DMSO) for 5 minutes prior to live imaging. Explants
469 treated with vehicle alone (DMSO only) were used for comparison. To examine the effects of
470 cyclodextrin on membrane dynamics and cytokinesis, explants were treated with 15 mM
471 methyl-β-cyclodextrin (solubilized in HL3.1) for 4 hours prior to live imaging. NSCs expressing
472 PH-GFP and Zeus-mCherry and incubated with methyl-β-cyclodextrin (n=10) or left untreated
473 (n=10) then imaged throughout mitosis and assessed by their ability to complete cytokinesis.
474
475 ***Immunofluorescent staining***
476 To determine the localization of native activated Moesin in NSCs, the central nervous systems
477 of third instar *Drosophila* larvae expressing Worniu-GAL4>UAS-PLCδ-PH-GFP were fixed in
478 4% paraformaldehyde. Mouse anti-GFP antibodies were used to stain neural stem cell

479 membranes (marked by Worniu-GAL4> UAS-PLCδ-PH-GFP), and rabbit anti-activated Moesin
480 antibodies were used to stain the phosphorylated form of Moesin. Primary antibodies were
481 used at a concentration of 1:100. Alexa 488 labeled anti-mouse (Invitrogen) and Alexa 555
482 labeled anti-rabbit (Invitrogen) secondary antibodies were used to stain GFP labeled neural
483 stem cell membranes and activated Moesin respectively. Super resolution images were
484 captured using a Nikon Eclipse Ti-2 (60x $H_2O$ objective) equipped with a Yokogawa CSU-W1
485 SoRa spinning disk head and dual Photometrics Prime BSI sCMOS cameras.
486
487 ***Image Processing and Analysis***
488 Images were analyzed using ImageJ (FIJI package) and Imaris (Bitplane) software. NSCs were
489 identified through their location in the brain and large size, as well as the presence of
490 transgenes expressed from the NSC specific promoter Worniu. 3D projections were created by
491 z-stack processing in ImageJ, using the maximum intensity projection method for standard
492 resolution imaging and standard deviation projection method for super resolution imaging.
493 Only optical sections from the front hemisphere of the NSC were used to create 3D
494 projections. We used a single optical section through the center of the cell along the apical-
495 basal axis as medial sections. Photobleaching during time-lapse imaging was corrected for
496 using ImageJ bleach correction tool in histogram matching mode. When image deconvolution
497 was applied, deconvolution was performed using Nikon Elements standard 2D deconvolution
498 mode. Image deconvolution was applied to Video S5 NSC #3. To reduce image noise,
499 Gaussian blur was applied to the Zeus-mCherry channel in Figure 6C and Video S9 using
500 ImageJ. Straightened membrane sections (Figure 5B) were prepared by manually tracing one
501 side of the NSC membrane from the apical pole to the cleavage furrow and applying the
502 straighten function in the ImageJ software package.
503
504 For the cell surface area quantifications in Figure 1E, cells expressing Miranda-GFP were used
505 to calculate the surface area of metaphase NSCs and each sibling cell immediately following
506 division. In ImageJ, a medial section was used to measure the diameter of the cell at five
507 different angles from which an average radius was obtained to be used in the following
508 calculations. The surface area was calculated with the equation $SA = 4\pi r^2$, where SA = surface
509 area and r = radius. From metaphase NSC images, the surface area of the nascent NP
510 membrane was calculated using the equation $2\pi rh$, where r = radius and h = height of the
511 Miranda marked cap. The surface area of the nascent NSC membrane was calculated by

512 subtracting the surface area of the nascent NP membrane from the total surface area of the
513 metaphase NSC. The surface area of the nascent NSC at metaphase was compared to the
514 surface area of the newly born NSC sibling immediately following division. Likewise, the
515 surface area of the nascent NP at metaphase was compared to the surface area of the newly
516 born NP sibling immediately following division.
517
518 To quantify the variations in thickness of the plasma membrane (Figure 1H), the thickness of
519 various regions of the plasma membrane was measured in NSCs marked with two different
520 membrane markers, UAS-farnesyl-GFP and UAS-PH-mCherry driven by Worniu-GAL4. Areas
521 of the membrane which had high signal intensity in both channels (relative to other regions of
522 the plasma membrane) were compared to areas of the membrane which exhibited average
523 signal intensity. Medial sections from seven different NSCs were used to measure the
524 thickness of the plasma membrane within areas of high signal intensity and also at four regions
525 of average signal intensity for each cell (totaling n=28 for each). Gardner-Altman estimation
526 plots for two group datasets and 95% confidence intervals of membrane thickness were
527 prepared using the DABEST package (Ho et al., 2019).
528
529 To quantify the thickness of membrane structures over time (Figure 5D), a z-stack of neural
530 stem cells expressing the membrane marker Worniu-GAL4>UAS-PLCδ-PH-GFP was acquired
531 every 20 seconds. The thickness of individual membrane domains was measured every 20
532 seconds for 300 seconds total starting at anaphase onset. To account for movement of the
533 membrane domain in the z-dimension, only the optical section with the thickest measurement
534 at each time point was used for quantification. The fold change in membrane domain thickness
535 for n = 15 membrane domains (n = 5 membrane domains from n = 3 neural stem cells from
536 distinct brain explants) was averaged and plotted using matplotlib.
537
538 To quantify membrane thickness at the apical and basal poles (Figures 2B, 4C, 5C, and 7C)
539 medial sections of NSCs were acquired using super resolution imaging. Images were loaded
540 into ImageJ, and a line which traversed the cell membrane at either the apical or basal pole
541 was drawn. If a cell junction between neighboring cells contacted the pole making it impossible
542 to measure the thickness of the neural stem cell membrane, a line which traversed the cell
543 membrane near to the pole but did not transect the cell junction was used. A plot profile was
544 generated and the signal intensity peak correlating to the cell membrane was identified based

545 on its position and high intensity over background signal. The length of the base of the peak
546 was measured to determine the thickness of the cell membrane. Measurements were taken at
547 various stages of the cell cycle and compared. When quantifying the effects of Gγ1 RNAi on
548 membrane thickness the same protocol was used, but only NSCs which divided symmetrically
549 were quantified. Gardner-Altman estimation plots for paired datasets and 95% confidence
550 intervals of membrane thickness were prepared using the DABEST package (Ho et al., 2019)
551 for n=5 NSCs from at least 3 separate brain explants.
552
553 ***Quantification and Statistical Analysis***
554 Gardner-Altman estimation plots and 95% confidence intervals of datasets were prepared
555 using the DABEST package (Ho et al., 2019). Statistical details can be found in the relevant
556 methods section and figure legend.
557
558 **Key Resources Table**

| REAGENT or RESOURCE | SOURCE | IDENTIFIER |
|---|---|---|
| Chemicals, Peptides, and Recombinant Proteins | | |
| Methyl-β-cyclodextrin | Caymen Chemical | Cat#21633<br>CAS# 128446-36-6 |
| Y27632<br>(Rho Kinase inhibitor) | Abcam | Cat#ab120129<br>CAS#129830-38-2 |
| Primary Antibodies | | |
| Anti-GFP | Developmental Studies Hybridoma Bank | Cat# DSHB-GFP-12A6 |
| Anti-Activated Moesin<br>(Phosphorylated Moesin; “p-Moesin”) | Cell Signaling Technology | Cat# 3726<br>Antibody#48G2 |
| Experimental Models: Fly Strains | | |
| Miranda-GFP | Jens Januschke Lab | |
| Myosin II-GFP (GFP tagged Spaghetti squash, the regulatory light chain of non-muscle type II Myosin) | (Royou et al., 2002) | |
| UAS-farnesyl-GFP<br>(“farnesyl-GFP” membrane marker) | Bloomington *Drosophila* Stock Center | BDSC Cat#80052<br>RRID:BDSC_80052 |
| UAS-Gγ1-RNAi<br>“Gγ RNAi” | Bloomington *Drosophila* Stock Center | BDSC Cat#34372<br>RRID:BDSC_34372 |
| UAS-GMA [GFP-Moesin-Actin binding domain]<br>(F-Actin marker) | Bloomington *Drosophila* Stock Center | BDSC Cat#31776<br>RRID:BDSC_31776 |
| UAS-PLCδ-PH-GFP<br>(“PH-GFP” membrane marker) | Bloomington *Drosophila* Stock Center | BDSC Cat#39693<br>RRID:BDSC_39693 |

| | | |
|---|---|---|
| UAS-PLCδ-PH-mCherry<br>(“PH-mCherry” membrane marker) | Bloomington *Drosophila* Stock Center | BDSC Cat#51658<br>RRID:BDSC_51658 |
| UAS-Zeus-mCherry<br>(microtubule marker) | Chris Q. Doe Lab | |
| Worniu-GAL4 | Chris Q. Doe Lab | |
| Software and Algorithms | | |
| Elements | Nikon | |
| ImageJ (FIJI package) | National Institutes of Health | |
| Imaris | Bitplane | |

561 **Video Legends**

562 Video S1: NSC membrane dynamics in early mitosis that lead to apical membrane reservoir
563 formation
564 Super resolution videos of PH-GFP (worniu-GAL4>UAS-PLCδ-PH-GFP; "membrane")
565 expressing NSCs in early mitosis shown in 3D projections and in medial sections.

566 Video S2: Correlated NSC membrane and cortical Actin dynamics in early mitosis
567 Super resolution videos of cortical F-Actin (worniu-GAL4>UAS-GMA; "F-Actin") and PH-
568 mCherry (worniu-GAL4>UAS-PLCδ-PH-mCherry; "membrane") expressing NSCs in early
569 mitosis shown in 3D projections and in medial sections.

570 Video S3: Correlated NSC membrane and Myosin II dynamics in early mitosis
571 Super resolution videos of GFP tagged Myosin type II (Myosin II) and PH-mCherry (worniu-
572 GAL4>UAS-PLCδ-PH-mCherry; "membrane") expressing NSCs in early mitosis shown in 3D
573 projections and in medial sections.

574 Video S4: Membrane dynamics in Rho Kinase inhibitor treated neural stem
575 cells
576 Super resolution videos of PH-GFP (worniu-GAL4>UAS-PLCδ-PH-GFP; "membrane") and
577 microtubules (worniu-GAL4>UAS-Zeus-mCherry; "microtubules") expressing NSCs in early
578 mitosis shown in 3D projections and in medial sections. Cells were treated with the Rho Kinase
579 inhibitor, Y27632 (NSCs 1-3) or vehicle (DMSO) alone (NSCs 4-6).

580 Video S5: Consumption of the apical membrane reservoir during anaphase expansion
581 Super resolution videos of PH-GFP (worniu-GAL4>UAS-PLCδ-PH-GFP; "membrane")
582 expressing NSCs during anaphase shown in 3D projections and in medial sections. "Close up
583 views" of the apical membrane are provided in NSCs 1-3. Image deconvolution was applied to
584 NSCs #3.

585 Video S6: NSC membrane dynamics during apical membrane reservoir formation and
586 consumption
587 Super resolution videos of PH-GFP (worniu-GAL4>UAS-PLCδ-PH-GFP; "membrane")
588 expressing NSCs during the entirety of mitosis in 3D projections and in medial sections.

589 Video S7: NSC membrane and cortical Actin dynamics during apical membrane reservoir
590 formation and consumption
591 Super resolution videos of cortical F-Actin (worniu-GAL4>UAS-GMA-GFP; “F-Actin”) and PH-
592 mCherry (worniu-GAL4>UAS-PLCδ-PH-mCherry; “membrane”) expressing NSCs during the
593 entirety of mitosis shown in 3D projections and in medial sections.

594 Video S8: NSC membrane and Myosin II dynamics during apical membrane reservoir
595 formation and consumption
596 Super resolution videos of GFP tagged Myosin II and PH-mCherry (worniu-GAL4>UAS-PLCδ-
597 PH-mCherry; “membrane”) expressing NSCs during the entirety of mitosis shown in 3D
598 projections and in medial sections.

599 Video S9: Membrane dynamics in cyclodextrin-treated NSCs
600 Super resolution videos of PH-GFP (worniu-GAL4>UAS-PLCδ-PH-GFP; “membrane”) and
601 microtubules (worniu-GAL4>UAS-Zeus-mCherry; ”microtubules”) expressing NSCs during the
602 entirety of mitosis shown in medial sections. Cells were treated with cyclodextrin (NSCs #1-4)
603 or untreated (NSC #5).

604 Video S10: Membrane dynamics in Gγ RNAi expressing NSCs
605 Super resolution (NSC #1) and standard resolution (NSCs #2 & 3) videos of PH-GFP (worniu-
606 GAL4>UAS-PLCδ-PH-GFP; “membrane”) and Gγ RNAi (worniu-GAL4>UAS-Gγ RNAi)
607 expressing NSCs shown in 3D projections and in medial sections.

608 **References**


609 Atwood SX, Prehoda KE. 2009. aPKC phosphorylates Miranda to polarize fate determinants
610 during neuroblast asymmetric cell division. *Curr Biol CB* **19**:723–729.
611 doi:10.1016/j.cub.2009.03.056
612 Azuma T, Kei T. 2015. Super-resolution spinning-disk confocal microscopy using optical
613 photon reassignment. *Opt Express* **23**:15003–15011. doi:10.1364/OE.23.015003
614 Barman S, Nayak DP. 2007. Lipid raft disruption by cholesterol depletion enhances influenza A
615 virus budding from MDCK cells. *J Virol* **81**:12169–12178. doi:10.1128/JVI.00835-07
616 Cabernard C, Prehoda KE, Doe CQ. 2010. A spindle-independent cleavage furrow positioning
617 pathway. *Nature* **467**:91–94. doi:10.1038/nature09334
618 Chakraborty S, Doktorova M, Molugu TR, Heberle FA, Scott HL, Dzikovski B, Nagao M,
619 Stingaciu L-R, Standaert RF, Barrera FN, Katsaras J, Khelashvili G, Brown MF, Ashkar
620 R. 2020. How cholesterol stiffens unsaturated lipid membranes. *Proc Natl Acad Sci U S*
621 *A* **117**:21896–21905. doi:10.1073/pnas.2004807117

622 Connell M, Cabernard C, Ricketson D, Doe CQ, Prehoda KE. 2011. Asymmetric cortical
623 extension shifts cleavage furrow position in Drosophila neuroblasts. *Mol Biol Cell*
624 **22**:4220–4226. doi:10.1091/mbc.E11-02-0173
625 Fehon RG, McClatchey AI, Bretscher A. 2010. Organizing the cell cortex: the role of ERM
626 proteins. *Nat Rev Mol Cell Biol* **11**:276–287. doi:10.1038/nrm2866
627 Figard L, Sokac AM. 2014. A membrane reservoir at the cell surface: unfolding the plasma
628 membrane to fuel cell shape change. *Bioarchitecture* **4**:39–46. doi:10.4161/bioa.29069
629 Figard L, Wang M, Zheng L, Golding I, Sokac AM. 2016. Membrane Supply and Demand
630 Regulates F-Actin in a Cell Surface Reservoir. *Dev Cell* **37**:267–278.
631 doi:10.1016/j.devcel.2016.04.010
632 Figard L, Xu H, Garcia HG, Golding I, Sokac AM. 2013. The plasma membrane flattens out to
633 fuel cell-surface growth during Drosophila cellularization. *Dev Cell* **27**:648–655.
634 doi:10.1016/j.devcel.2013.11.006
635 Gallaud E, Pham T, Cabernard C. 2017. Drosophila melanogaster Neuroblasts: A Model for
636 Asymmetric Stem Cell Divisions. *Results Probl Cell Differ* **61**:183–210. doi:10.1007/978-
637 3-319-53150-2_8
638 Goudarzi M, Tarbashevich K, Mildner K, Begemann I, Garcia J, Paksa A, Reichman-Fried M,
639 Mahabaleshwar H, Blaser H, Hartwig J, Zeuschner D, Galic M, Bagnat M, Betz T, Raz E.
640 2017. Bleb Expansion in Migrating Cells Depends on Supply of Membrane from Cell
641 Surface Invaginations. *Dev Cell* **43**:577-587.e5. doi:10.1016/j.devcel.2017.10.030
642 Hirani N, Illukkumbura R, Bland T, Mathonnet G, Suhner D, Reymann A-C, Goehring NW. 2019.
643 Anterior-enriched filopodia create the appearance of asymmetric membrane
644 microdomains in polarizing C. elegans zygotes. *J Cell Sci* **132**. doi:10.1242/jcs.230714
645 Ho J, Tumkaya T, Aryal S, Choi H, Claridge-Chang A. 2019. Moving beyond P values: data
646 analysis with estimation graphics. *Nat Methods* **16**:565–566. doi:10.1038/s41592-019-
647 0470-3
648 Homem CCF, Knoblich JA. 2012. Drosophila neuroblasts: a model for stem cell biology
649 **139**:4297–4310. doi:10.1242/dev.080515
650 Illukkumbura R, Bland T, Goehring NW. 2019. Patterning and polarization of cells by
651 intracellular flows. *Curr Opin Cell Biol* **62**:123–134. doi:10.1016/j.ceb.2019.10.005
652 Izumi Y, Ohta N, Itoh-Furuya A, Fuse N, Matsuzaki F. 2004. Differential functions of G protein
653 and Baz-aPKC signaling pathways in Drosophila neuroblast asymmetric division. *J Cell*
654 *Biol* **164**:729–738. doi:10.1083/jcb.200309162
655 Kabeche R, Howard L, Moseley JB. 2015. Eisosomes provide membrane reservoirs for rapid
656 expansion of the yeast plasma membrane. *J Cell Sci* **128**:4057–4062.
657 doi:10.1242/jcs.176867
658 Knoblich JA. 2010. Asymmetric cell division: recent developments and their implications for
659 tumour biology. *Nat Rev Mol Cell Biol* **11**:849–860. doi:10.1038/nrm3010
660 Knoblich JA. 2008. Mechanisms of asymmetric stem cell division. *Cell* **132**:583–597.
661 doi:10.1016/j.cell.2008.02.007
662 Kornberg TB. 2014. Cytonemes and the dispersion of morphogens. *Wiley Interdiscip Rev Dev*
663 *Biol* **3**:445–463. doi:10.1002/wdev.151
664 LaFoya B, Prehoda KE. 2021. Actin-dependent membrane polarization reveals the mechanical
665 nature of the neuroblast polarity cycle. *Cell Rep* **35**:109146.
666 doi:10.1016/j.celrep.2021.109146
667 Lang CF, Munro E. 2017. The PAR proteins: from molecular circuits to dynamic self-stabilizing
668 cell polarity. *Dev Camb Engl* **144**:3405–3416. doi:10.1242/dev.139063

669 Meenderink LM, Gaeta IM, Postema MM, Cencer CS, Chinowsky CR, Krystofiak ES, Millis BA,
670 Tyska MJ. 2019. Actin Dynamics Drive Microvillar Motility and Clustering during Brush
671 Border Assembly. *Dev Cell* **50**:545-556.e4. doi:10.1016/j.devcel.2019.07.008
672 Munro E, Nance J, Priess JR. 2004. Cortical flows powered by asymmetrical contraction
673 transport PAR proteins to establish and maintain anterior-posterior polarity in the early
674 C. elegans embryo. *Dev Cell* **7**:413–424. doi:10.1016/j.devcel.2004.08.001
675 Oon CH, Prehoda KE. 2021. Phases of cortical actomyosin dynamics coupled to the
676 neuroblast polarity cycle. *eLife* **10**:e66574. doi:10.7554/eLife.66574
677 Oon CH, Prehoda KE. 2019. Asymmetric recruitment and actin-dependent cortical flows drive
678 the neuroblast polarity cycle. *eLife* **8**. doi:10.7554/eLife.45815
679 Pang DJ, Hayday AC, Bijlmakers M-J. 2007. CD8 Raft Localization Is Induced by Its Assembly
680 into CD8αβ Heterodimers, Not CD8αα Homodimers. *J Biol Chem* **282**:13884–13894.
681 doi:10.1074/jbc.M701027200
682 Pham TT, Monnard A, Helenius J, Lund E, Lee N, Müller DJ, Cabernard C. 2019.
683 Spatiotemporally Controlled Myosin Relocalization and Internal Pressure Generate
684 Sibling Cell Size Asymmetry. *iScience* **13**:9–19. doi:10.1016/j.isci.2019.02.002
685 Ramat A, Hannaford M, Januschke J. 2017. Maintenance of Miranda Localization in Drosophila
686 Neuroblasts Involves Interaction with the Cognate mRNA. *Curr Biol CB* **27**:2101-
687 2111.e5. doi:10.1016/j.cub.2017.06.016
688 Roth M, Roubinet C, Iffländer N, Ferrand A, Cabernard C. 2015. Asymmetrically dividing
689 Drosophila neuroblasts utilize two spatially and temporally independent cytokinesis
690 pathways. *Nat Commun* **6**:6551. doi:10.1038/ncomms7551
691 Roubinet C, Tsankova A, Pham TT, Monnard A, Caussinus E, Affolter M, Cabernard C. 2017.
692 Spatio-temporally separated cortical flows and spindle geometry establish physical
693 asymmetry in fly neural stem cells. *Nat Commun* **8**:1383. doi:10.1038/s41467-017-
694 01391-w
695 Royou A, Sullivan W, Karess R. 2002. Cortical recruitment of nonmuscle myosin II in early
696 syncytial Drosophila embryos: its role in nuclear axial expansion and its regulation by
697 Cdc2 activity. *J Cell Biol* **158**:127–137. doi:10.1083/jcb.200203148
698 Scholze MJ, Barbieux KS, De Simone A, Boumasmoud M, Süess CCN, Wang R, Gönczy P.
699 2018. PI(4,5)P2 forms dynamic cortical structures and directs actin distribution as well
700 as polarity in Caenorhabditis elegans embryos. *Dev Camb Engl* **145**.
701 doi:10.1242/dev.164988
702 Sokac AM. 2017. Seeing a Coastline Paradox in Membrane Reservoirs. *Dev Cell* **43**:541–542.
703 doi:10.1016/j.devcel.2017.11.013
704

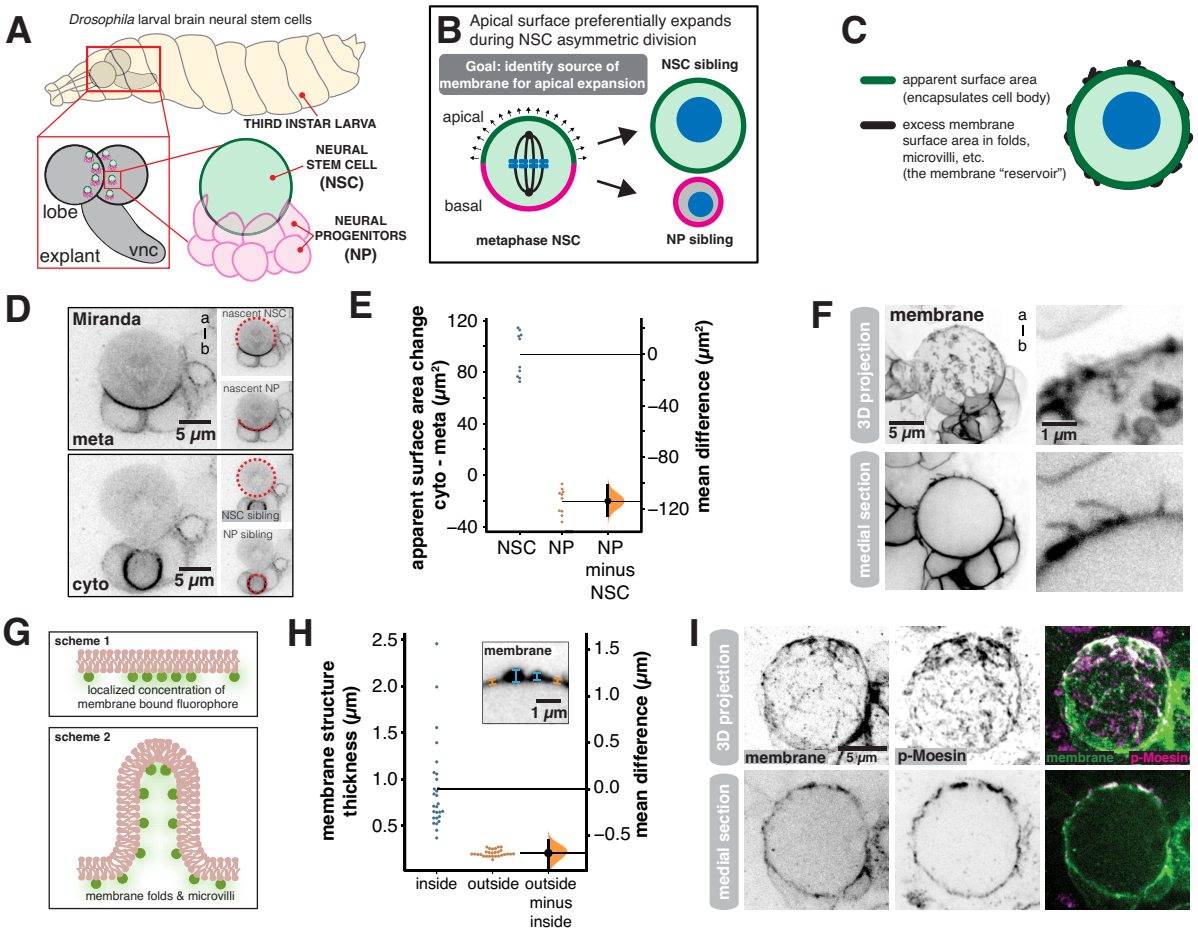
A
Drosophila larval brain neural stem cells
THIRD INSTAR LARVA
NEURAL STEM CELL (NSC)
NEURAL PROGENITORS (NP)
lobe
vnc
explant
B
Apical surface preferentially expands during NSC asymmetric division
Goal: identify source of membrane for apical expansion
apical
basal
metaphase NSC
NSC sibling
NP sibling
C
apparent surface area (encapsulates cell body)
excess membrane surface area in folds, microvilli, etc. (the membrane "reservoir")
D
Miranda
a
l
b
nascent NSC
nascent NP
meta
5 μm
NSC sibling
NP sibling
cyto
5 μm
E
apparent surface area change cyto - meta (μm²)
mean difference (μm²)
NSC
NP
NP minus NSC
F
membrane
3D projection
medial section
5 μm
1 μm
G
scheme 1
localized concentration of membrane bound fluorophore
scheme 2
membrane folds & microvilli
H
membrane structure thickness (μm)
mean difference (μm)
membrane
1 μm
inside
outside
outside minus inside
I
3D projection
medial section
membrane
5 μm
p-Moesin
membrane
p-Moesin

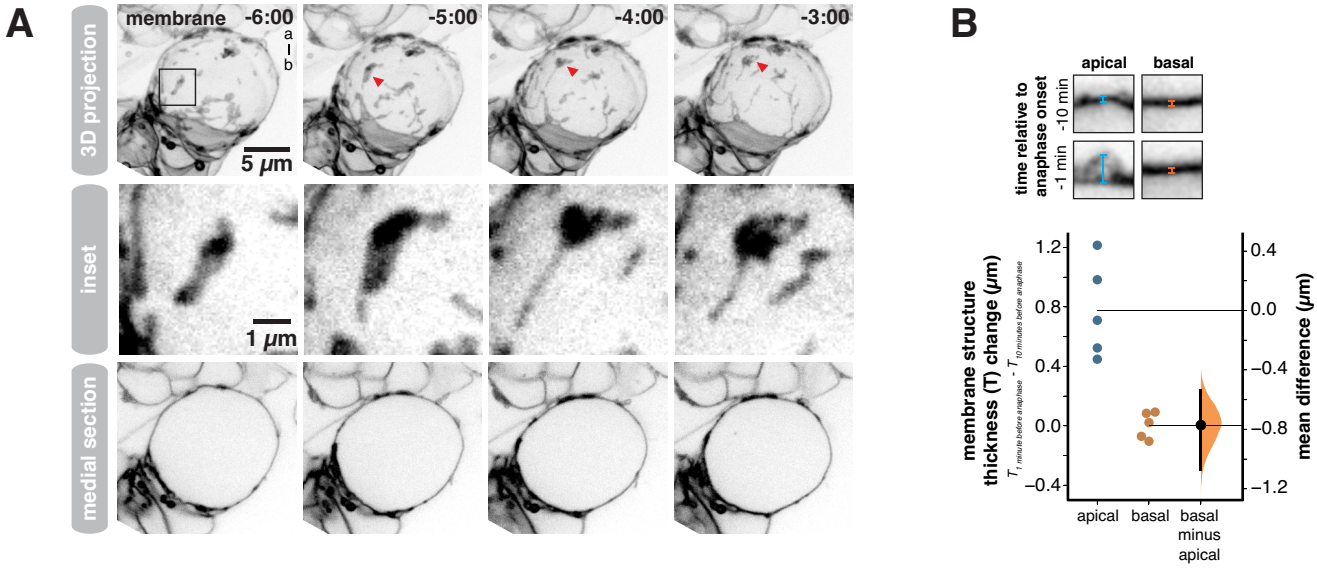
A
3D projection
inset
medial section
membrane
-6:00
-5:00
-4:00
-3:00
a
l
b
5 μm
1 μm
B
apical
basal
time relative to anaphase onset
-10 min
-1 min
membrane structure thickness (T) change (μm)
mean difference (μm)
1.2
0.8
0.4
0.0
−0.4
0.4
0.0
−0.4
−0.8
−1.2
apical
basal
basal minus apical

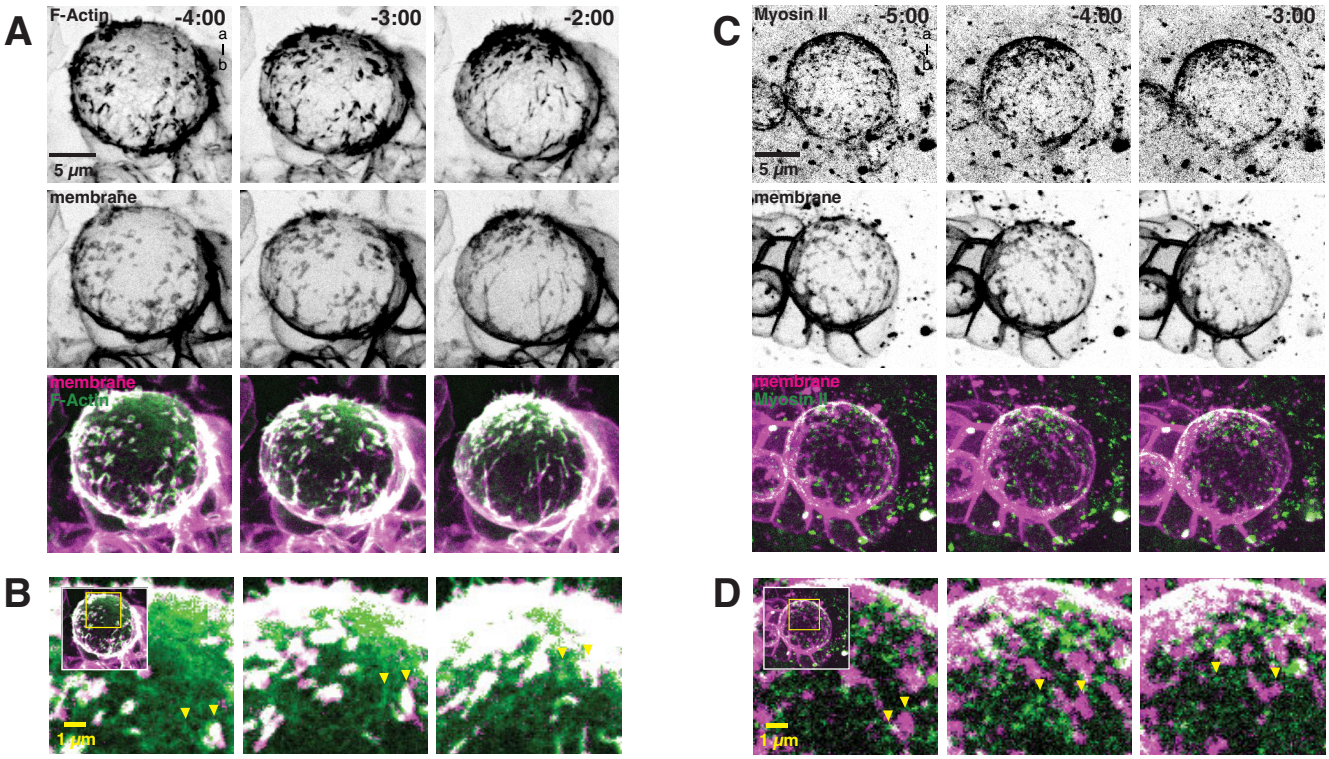
A
F-Actin
-4:00
-3:00
-2:00
a
l
b
5 µm
membrane
membrane
F-Actin
B
1 µm
C
Myosin II
-5:00
-4:00
-3:00
a
l
b
5 µm
membrane
membrane
Myosin II
D
1 µm

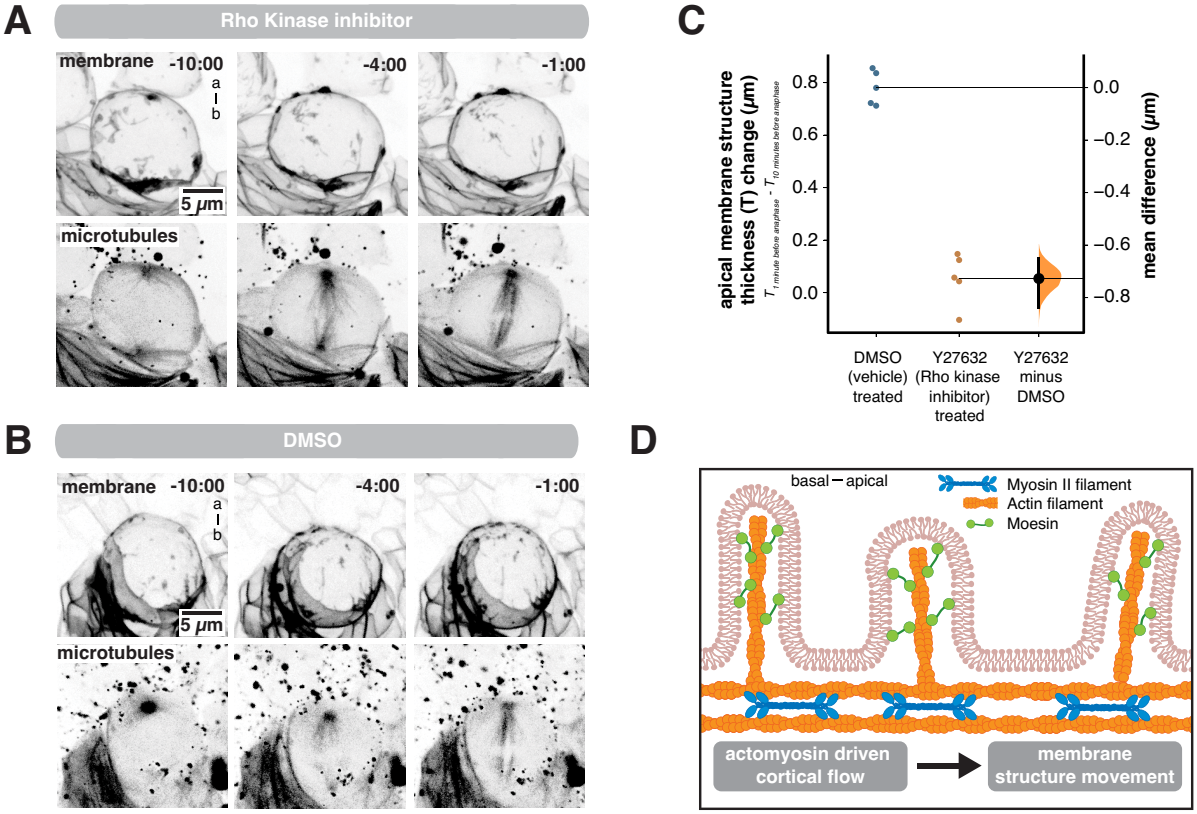
A
Rho Kinase inhibitor
membrane
-10:00
a
l
b
-4:00
-1:00
5 μm
microtubules
B
DMSO
membrane
-10:00
a
l
b
-4:00
-1:00
5 μm
microtubules
C
apical membrane structure thickness (T) change (μm)
T 1 minute before anaphase - T 10 minutes before anaphase
0.8
0.6
0.4
0.2
0.0
0.0
−0.2
−0.4
−0.6
−0.8
mean difference (μm)
DMSO (vehicle) treated
Y27632 (Rho kinase inhibitor) treated
Y27632 minus DMSO
D
basal — apical
Myosin II filament
Actin filament
Moesin
actomyosin driven cortical flow
membrane structure movement

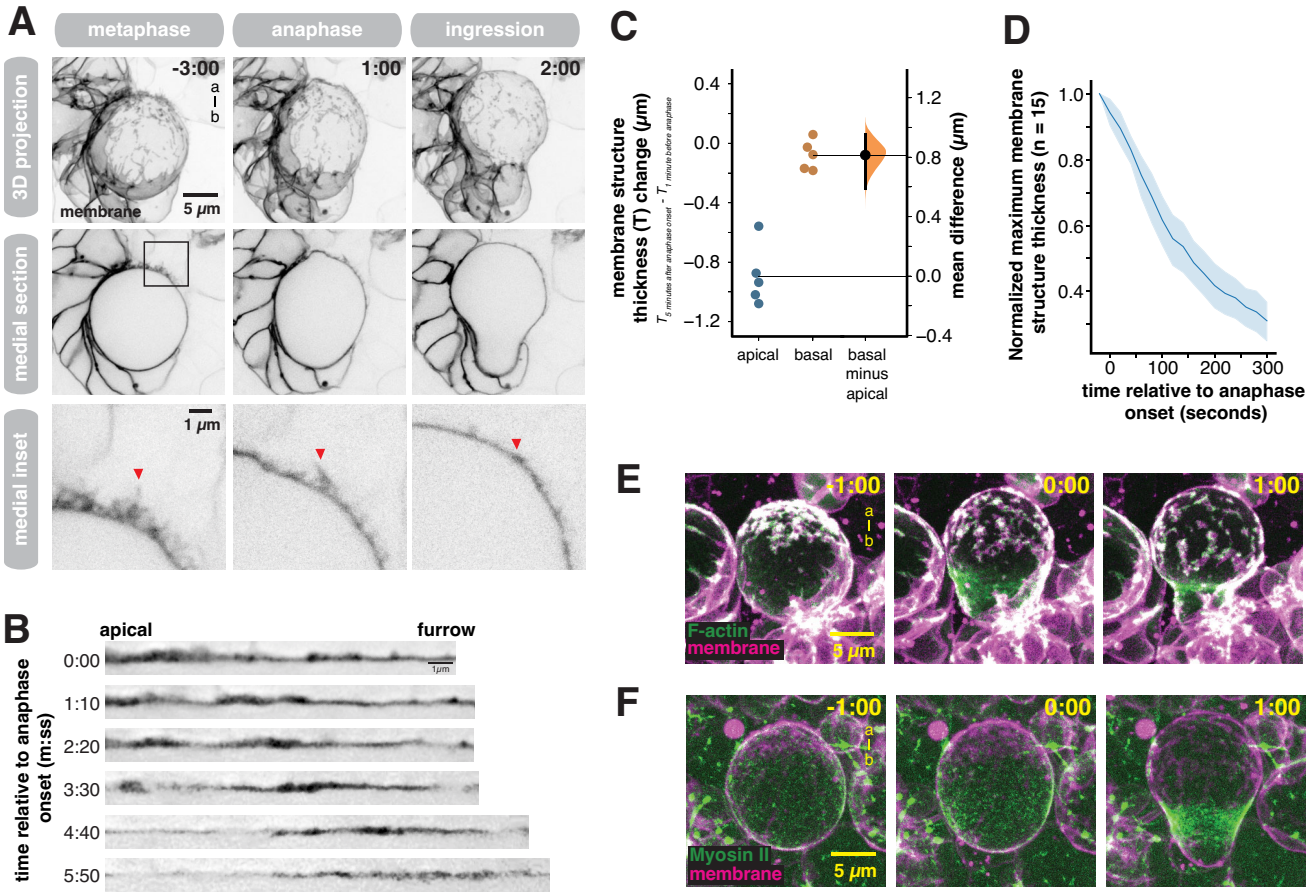
A
metaphase
anaphase
ingression
3D projection
medial section
medial inset
-3:00
1:00
2:00
a
b
membrane
5 µm
1 µm
B
apical
furrow
time relative to anaphase onset (m:ss)
0:00
1:10
2:20
3:30
4:40
5:50
C
membrane structure thickness (T) change (µm)
mean difference (µm)
apical
basal
basal minus apical
D
Normalized maximum membrane structure thickness (n = 15)
time relative to anaphase onset (seconds)
E
-1:00
0:00
1:00
F-actin
membrane
5 µm
F
Myosin II
membrane

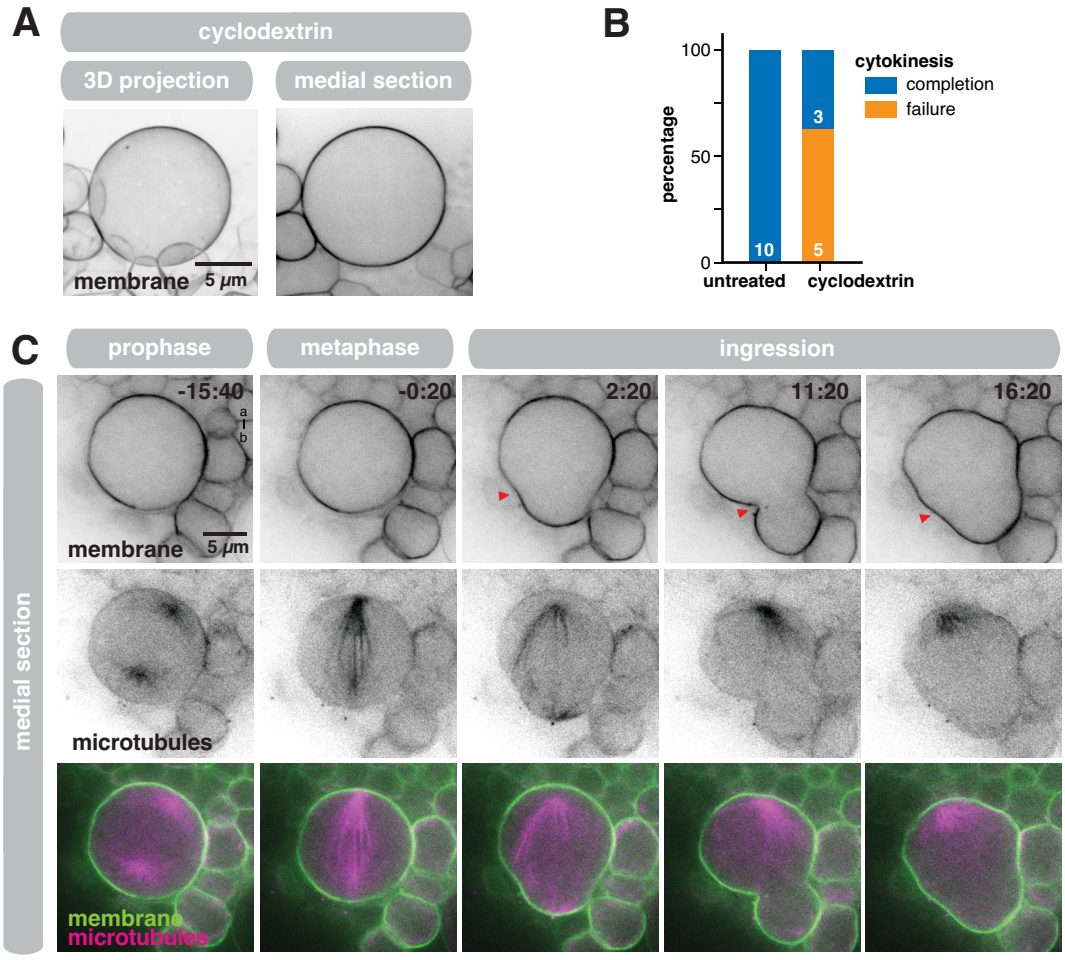
A
cyclodextrin
3D projection
medial section
membrane
5 μm
B
100
50
0
percentage
cytokinesis
completion
failure
3
10
5
untreated
cyclodextrin
C
prophase
metaphase
ingression
medial section
-15:40
a
b
-0:20
2:20
11:20
16:20
membrane
5 μm
microtubules
membrane
microtubules

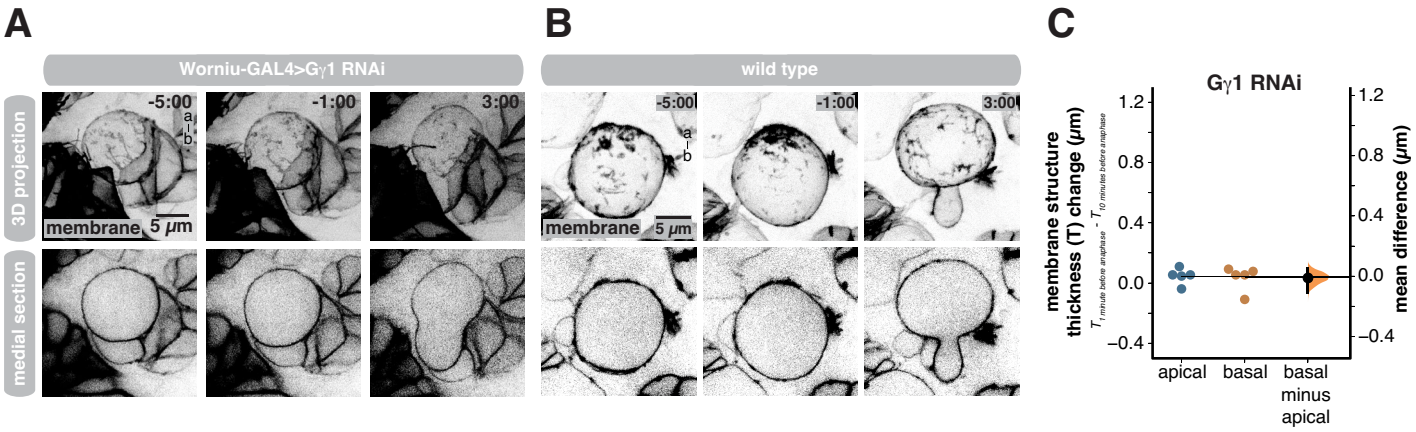
A
Worniu-GAL4>Gγ1 RNAi
3D projection
medial section
-5:00
-1:00
3:00
a
b
membrane
5 μm
B
wild type
-5:00
-1:00
3:00
a
b
membrane
5 μm
C
Gγ1 RNAi
membrane structure thickness (T) change (μm)
T 1 minute before anaphase - T 10 minutes before anaphase
mean difference (μm)
1.2
0.8
0.4
0.0
−0.4
apical
basal
basal minus apical

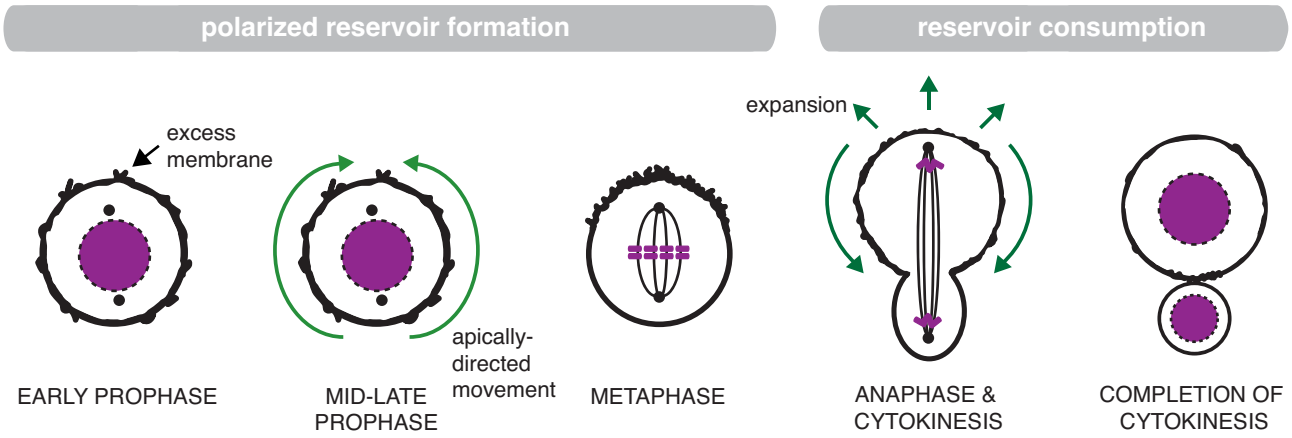
polarized reservoir formation
reservoir consumption
excess membrane
apically-directed movement
expansion
EARLY PROPHASE
MID-LATE PROPHASE
METAPHASE
ANAPHASE & CYTOKINESIS
COMPLETION OF CYTOKINESIS